High-resolution 1050 nm spectral domain retinal optical coherence tomography at 120 kHz A-scan rate with 6.1 mm imaging depth

Lin An,[1] Peng Li,[1] Gongpu Lan,[1] Doug Malchow,[2] and Ruikang K. Wang[1,*]

[1]*Department of Bioengineering, University of Washington, Seattle, WA 98195, USA*
[2]*Sensors Unlimited Inc (SUI), Princeton, NJ 08540, USA*
*wangrk@uw.edu

Abstract: We report a newly developed high speed 1050nm spectral domain optical coherence tomography (SD-OCT) system for imaging posterior segment of human eye. The system is capable of an axial resolution at ~10 µm in air, an imaging depth of 6.1 mm in air, a system sensitivity fall-off at ~6 dB/3mm and an imaging speed of 120,000 A-scans per second. We experimentally demonstrate the system's capability to perform phase-resolved imaging of dynamic blood flow within retina, indicating high phase stability of the SDOCT system. Finally, we show an example that uses this newly developed system to image posterior segment of human eye with a large view of view (10×9 mm^2), providing detailed visualization of microstructural features from anterior retina to posterior choroid. The demonstrated system parameters and imaging performances are comparable to those that a typical 1 µm swept source OCT would deliver for retinal imaging.

© 2013 Optical Society of America

OCIS codes: (170.4460) Ophthalmic optics and devices; (170.3880) Medical and biological imaging; (170.4500) Optical coherence tomography.

References and Links

1. A. F. Fercher, C. K. Hitzenberger, W. Drexler, G. Kamp, and H. Sattmann, "In vivo optical coherence tomography," Am. J. Ophthalmol. **116**(1), 113–114 (1993).
2. P. H. Tomlins and R. K. Wang, "Theory, developments and applications of optical coherence tomography," J. Phys. D Appl. Phys. **38**(15), 2519–2535 (2005).
3. C. K. Hitzenberger, P. Trost, P. W. Lo, and Q. Y. Zhou, "Three-dimensional imaging of the human retina by high-speed optical coherence tomography," Opt. Express **11**(21), 2753–2761 (2003).
4. A. M. Rollins, S. Yazdanfar, M. Kulkarni, R. Ung-Arunyawee, and J. A. Izatt, "In vivo video rate optical coherence tomography," Opt. Express **3**(6), 219–229 (1998).
5. A. F. Fercher, C. K. Hitzenberger, G. Kamp, and S. Y. Elzaiat, "Measurement of intraocular distances by backscattering spectral interferometry," Opt. Commun. **117**(1-2), 43–48 (1995).
6. G. Häusler and M. W. Lindner, ""Coherence radar" and "spectral radar"-new tools for dermatological diagnosis," J. Biomed. Opt. **3**(1), 21–31 (1998).
7. S. R. Chinn, E. A. Swanson, and J. G. Fujimoto, "Optical coherence tomography using a frequency-tunable optical source," Opt. Lett. **22**(5), 340–342 (1997).
8. U. Haberland, P. Jansen, V. Blazek, and H. J. Schmitt, "Optical coherence tomography of scattering media using frequency-modulated continuous-wave techniques with tunable near-infrared laser," Proc. SPIE **2891**, 20–28 (1997).
9. R. Leitgeb, C. K. Hitzenberger, and A. F. Fercher, "Performance of fourier domain vs. time domain optical coherence tomography," Opt. Express **11**(8), 889–894 (2003).
10. J. F. de Boer, B. Cense, B. H. Park, M. C. Pierce, G. J. Tearney, and B. E. Bouma, "Improved signal-to-noise ratio in spectral-domain compared with time-domain optical coherence tomography," Opt. Lett. **28**(21), 2067–2069 (2003).
11. M. Choma, M. Sarunic, C. Yang, and J. Izatt, "Sensitivity advantage of swept source and Fourier domain optical coherence tomography," Opt. Express **11**(18), 2183–2189 (2003).
12. B. Cense, N. Nassif, T. Chen, M. Pierce, S.-H. Yun, B. Park, B. Bouma, G. Tearney, and J. de Boer, "Ultrahigh-resolution high-speed retinal imaging using spectral-domain optical coherence tomography," Opt. Express **12**(11), 2435–2447 (2004).

13. D. M. de Bruin, D. L. Burnes, J. Loewenstein, Y. Chen, S. Chang, T. C. Chen, D. D. Esmaili, and J. F. de Boer, "In vivo three-dimensional imaging of neovascular age-related macular degeneration using optical frequency domain imaging at 1050 nm," Invest. Ophthalmol. Vis. Sci. **49**(10), 4545–4552 (2008).
14. E. C. Lee, J. F. de Boer, M. Mujat, H. Lim, and S. H. Yun, "In vivo optical frequency domain imaging of human retina and choroid," Opt. Express **14**(10), 4403–4411 (2006).
15. H. Lim, M. Mujat, C. Kerbage, E. C. Lee, Y. Chen, T. C. Chen, and J. F. de Boer, "High-speed imaging of human retina in vivo with swept-source optical coherence tomography," Opt. Express **14**(26), 12902–12908 (2006).
16. M. Wojtkowski, V. Srinivasan, T. Ko, J. Fujimoto, A. Kowalczyk, and J. Duker, "Ultrahigh-resolution, high-speed, Fourier domain optical coherence tomography and methods for dispersion compensation," Opt. Express **12**(11), 2404–2422 (2004).
17. R. A. Leitgeb, W. Drexler, A. Unterhuber, B. Hermann, T. Bajraszewski, T. Le, A. Stingl, and A. F. Fercher, "Ultrahigh resolution Fourier domain optical coherence tomography," Opt. Express **12**(10), 2156–2165 (2004).
18. V. J. Srinivasan, R. Huber, I. Gorczynska, J. G. Fujimoto, J. Y. Jiang, P. Reisen, and A. E. Cable, "High-speed, high-resolution optical coherence tomography retinal imaging with a frequency-swept laser at 850 nm," Opt. Lett. **32**(4), 361–363 (2007).
19. A. H. Bachmann, M. L. Villiger, C. Blatter, T. Lasser, and R. A. Leitgeb, "Resonant Doppler flow imaging and optical vivisection of retinal blood vessels," Opt. Express **15**(2), 408–422 (2007).
20. L. An and R. K. Wang, "In vivo volumetric imaging of vascular perfusion within human retina and choroids with optical micro-angiography," Opt. Express **16**(15), 11438–11452 (2008).
21. B. J. Vakoc, R. M. Lanning, J. A. Tyrrell, T. P. Padera, L. A. Bartlett, T. Stylianopoulos, L. L. Munn, G. J. Tearney, D. Fukumura, R. K. Jain, and B. E. Bouma, "Three-dimensional microscopy of the tumor microenvironment in vivo using optical frequency domain imaging," Nat. Med. **15**(10), 1219–1223 (2009).
22. B. R. White, M. C. Pierce, N. Nassif, B. Cense, B. H. Park, G. J. Tearney, B. E. Bouma, T. C. Chen, and J. de Boer, "In vivo dynamic human retinal blood flow imaging using ultra-high-speed spectral domain optical coherence tomography," Opt. Express **11**(25), 3490–3497 (2003).
23. J. Fingler, R. J. Zawadzki, J. S. Werner, D. Schwartz, and S. E. Fraser, "Volumetric microvascular imaging of human retina using optical coherence tomography with a novel motion contrast technique," Opt. Express **17**(24), 22190–22200 (2009).
24. L. An, H. M. Subhush, D. J. Wilson, and R. K. Wang, "High-resolution wide-field imaging of retinal and choroidal blood perfusion with optical microangiography," J. Biomed. Opt. **15**(2), 026011 (2010).
25. L. Yu and Z. Chen, "Doppler variance imaging for three-dimensional retina and choroid angiography," J. Biomed. Opt. **15**(1), 016029 (2010).
26. M. Szkulmowski, A. Szkulmowska, T. Bajraszewski, A. Kowalczyk, and M. Wojtkowski, "Flow velocity estimation using joint spectral and time domain optical coherence tomography," Opt. Express **16**(9), 6008–6025 (2008).
27. R. K. Wang, L. An, S. Saunders, and D. J. Wilson, "Optical microangiography provides depth-resolved images of directional ocular blood perfusion in posterior eye segment," J. Biomed. Opt. **15**(2), 020502 (2010).
28. S. Makita, F. Jaillon, M. Yamanari, M. Miura, and Y. Yasuno, "Comprehensive in vivo micro-vascular imaging of the human eye by dual-beam-scan Doppler optical coherence angiography," Opt. Express **19**(2), 1271–1283 (2011).
29. S. Makita, Y. Hong, M. Yamanari, T. Yatagai, and Y. Yasuno, "Optical coherence angiography," Opt. Express **14**(17), 7821–7840 (2006).
30. B. Potsaid, B. Baumann, D. Huang, S. Barry, A. E. Cable, J. S. Schuman, J. S. Duker, and J. G. Fujimoto, "Ultrahigh speed 1050nm swept source/Fourier domain OCT retinal and anterior segment imaging at 100,000 to 400,000 axial scans per second," Opt. Express **18**(19), 20029–20048 (2010).
31. C. M. Eigenwillig, T. Klein, W. Wieser, B. R. Biedermann, and R. Huber, "Wavelength swept amplified spontaneous emission source for high speed retinal optical coherence tomography at 1060 nm," J Biophotonics **4**(7-8), 552–558 (2011).
32. T. Klein, W. Wieser, C. M. Eigenwillig, B. R. Biedermann, and R. Huber, "Megahertz OCT for ultrawide-field retinal imaging with a 1050nm Fourier domain mode-locked laser," Opt. Express **19**(4), 3044–3062 (2011).
33. M. Gora, K. Karnowski, M. Szkulmowski, B. J. Kaluzny, R. Huber, A. Kowalczyk, and M. Wojtkowski, "Ultra high-speed swept source OCT imaging of the anterior segment of human eye at 200 kHz with adjustable imaging range," Opt. Express **17**(17), 14880–14894 (2009).
34. V. J. Srinivasan, D. C. Adler, Y. Chen, I. Gorczynska, R. Huber, J. S. Duker, J. S. Schuman, and J. G. Fujimoto, "Ultrahigh-speed optical coherence tomography for three-dimensional and en face imaging of the retina and optic nerve head," Invest. Ophthalmol. Vis. Sci. **49**(11), 5103–5110 (2008).
35. B. Potsaid, I. Gorczynska, V. J. Srinivasan, Y. L. Chen, J. Jiang, A. Cable, and J. G. Fujimoto, "Ultrahigh speed spectral / Fourier domain OCT ophthalmic imaging at 70,000 to 312,500 axial scans per second," Opt. Express **16**(19), 15149–15169 (2008).
36. D. Y. Kim, J. Fingler, J. S. Werner, D. M. Schwartz, S. E. Fraser, and R. J. Zawadzki, "In vivo volumetric imaging of human retinal circulation with phase-variance optical coherence tomography," Biomed. Opt. Express **2**(6), 1504–1513 (2011).
37. R. K. Wang, L. An, P. Francis, and D. J. Wilson, "Depth-resolved imaging of capillary networks in retina and choroid using ultrahigh sensitive optical microangiography," Opt. Lett. **35**(9), 1467–1469 (2010).

38. L. An, P. Li, T. T. Shen, and R. K. Wang, "High speed spectral domain optical coherence tomography for retinal imaging at 500,000 A-lines per second," Biomed. Opt. Express **2**(10), 2770–2783 (2011).
39. Y. Wang, J. Nelson, Z. Chen, B. Reiser, R. Chuck, and R. Windeler, "Optimal wavelength for ultrahigh-resolution optical coherence tomography," Opt. Express **11**(12), 1411–1417 (2003).
40. J. Xi, L. Huo, J. Li, and X. Li, "Generic real-time uniform K-space sampling method for high-speed swept-source optical coherence tomography," Opt. Express **18**(9), 9511–9517 (2010).
41. W. Wieser, B. R. Biedermann, T. Klein, C. M. Eigenwillig, and R. Huber, "Multi-megahertz OCT: High quality 3D imaging at 20 million A-scans and 4.5 GVoxels per second," Opt. Express **18**(14), 14685–14704 (2010).
42. R. K. Manapuram, V. G. R. Manne, and K. V. Larin, "Development of phase-stabilized swept-source OCT for the ultrasensitive quantification of microbubbles," Laser Phys. **18**(9), 1080–1086 (2008).
43. H. C. Hendargo, R. P. McNabb, A. H. Dhalla, N. Shepherd, and J. A. Izatt, "Doppler velocity detection limitations in spectrometer-based versus swept-source optical coherence tomography," Biomed. Opt. Express **2**(8), 2175–2188 (2011).
44. B. Braaf, K. A. Vermeer, V. A. Sicam, E. van Zeeburg, J. C. van Meurs, and J. F. de Boer, "Phase-stabilized optical frequency domain imaging at 1-μm for the measurement of blood flow in the human choroid," Opt. Express **19**(21), 20886–20903 (2011).
45. B. J. Vakoc, S. H. Yun, J. F. de Boer, G. J. Tearney, and B. E. Bouma, "Phase-resolved optical frequency domain imaging," Opt. Express **13**(14), 5483–5493 (2005).
46. J. Zhang and Z. Chen, "In vivo blood flow imaging by a swept laser source based Fourier domain optical Doppler tomography," Opt. Express **13**(19), 7449–7457 (2005).
47. B. Baumann, B. Potsaid, M. F. Kraus, J. J. Liu, D. Huang, J. Hornegger, A. E. Cable, J. S. Duker, and J. G. Fujimoto, "Total retinal blood flow measurement with ultrahigh speed swept source/Fourier domain OCT," Biomed. Opt. Express **2**(6), 1539–1552 (2011).
48. Y. J. Hong, S. Makita, F. Jaillon, M. J. Ju, E. J. Min, B. H. Lee, M. Itoh, M. Miura, and Y. Yasuno, "High-penetration swept source Doppler optical coherence angiography by fully numerical phase stabilization," Opt. Express **20**(3), 2740–2760 (2012).
49. R. K. Wang and L. An, "Multifunctional imaging of human retina and choroid with 1050-nm spectral domain optical coherence tomography at 92-kHz line scan rate," J. Biomed. Opt. **16**(5), 050503 (2011).
50. American National Standard Institute," Safe use of lasers and safe use of optical fiber communications," (ANSI, New York; 2000), no. 168.
51. Y. Zhao, Z. Chen, Z. Ding, H. Ren, and J. S. Nelson, "Real-time phase-resolved functional optical coherence tomography by use of optical Hilbert transformation," Opt. Lett. **27**(2), 98–100 (2002).
52. R. K. Wang and Z. Ma, "Real-time flow imaging by removing texture pattern artifacts in spectral-domain optical Doppler tomography," Opt. Lett. **31**(20), 3001–3003 (2006).
53. R. K. Wang, Z. Ma, and S. J. Kirkpatrick, "Tissue Doppler optical coherence elastography for real time strain rate and strain mapping of soft tissue," Appl. Phys. Lett. **89**, 3 (2006).
54. D. C. Adler, S. W. Huang, R. Huber, and J. G. Fujimoto, "Photothermal detection of gold nanoparticles using phase-sensitive optical coherence tomography," Opt. Express **16**(7), 4376–4393 (2008).
55. Y. Jung, R. Reif, Y. Zeng, and R. K. Wang, "Three-dimensional high-resolution imaging of gold nanorods uptake in sentinel lymph nodes," Nano Lett. **11**(7), 2938–2943 (2011).
56. R. K. Wang and A. L. Nuttall, "Phase-sensitive optical coherence tomography imaging of the tissue motion within the organ of Corti at a subnanometer scale: a preliminary study," J. Biomed. Opt. **15**(5), 056005 (2010).
57. G. Fuchsjäger-Mayrl, B. Wally, M. Georgopoulos, G. Rainer, K. Kircher, W. Buehl, T. Amoako-Mensah, H. G. Eichler, C. Vass, and L. Schmetterer, "Ocular blood flow and systemic blood pressure in patients with primary open-angle glaucoma and ocular hypertension," Invest. Ophthalmol. Vis. Sci. **45**(3), 834–839 (2004).
58. V. Patel, S. Rassam, R. Newsom, J. Wiek, and E. Kohner, "Retinal blood flow in diabetic retinopathy," BMJ **305**(6855), 678–683 (1992).
59. E. Sato, G. T. Feke, M. N. Menke, and J. Wallace McMeel, "Retinal haemodynamics in patients with age-related macular degeneration," Eye (Lond.) **20**(6), 697–702 (2006).
60. B. Rao, L. Yu, H. K. Chiang, L. C. Zacharias, R. M. Kurtz, B. D. Kuppermann, and Z. Chen, "Imaging pulsatile retinal blood flow in human eye," J. Biomed. Opt. **13**(4), 040505 (2008).

1. Introduction

Optical coherence tomography (OCT) [1,2] is a non-invasive, non-contact, high-resolution, high-sensitive and depth-resolved optical imaging modality, which has been widely applied in many biomedical imaging fields such as ophthalmology, dermatology, cardiology and embryology. Among all these applications, the ophthalmic application is the most successful one, where OCT has become a routine tool for diagnosis or monitoring of several major eye diseases, such as age-related macular degeneration, glaucoma, diabetic retinopathy and others. Over the recent years, rapid development of OCT has resulted in great improvement in system imaging performances, manifested by its capability to provide comprehensive 3D imaging data set for more accurate diagnosis and with an imaging time within a fraction of one second. The

relatively shorter imaging time is important because it makes it possible for patients to have more comfortable examination experiences while minimizing motion artifacts.

To date, the development of OCT technology may be roughly divided into three generations. The first generation OCT is the time domain OCT (TD-OCT) [1], in which mechanical scanning is usually employed to achieve depth-resolved imaging. Due to the limitation of the mechanical scanning, TD-OCT is only capable of achieving an imaging speed of several thousand A-lines per second, making it difficult to realize 3D scanning for *in vivo* human eye examinations [3,4]. The second generation OCT is the Fourier domain OCT (FD-OCT). FD-OCT achieves the depth resolved imaging through applying fast Fourier transform to the detected spectral interferogram [5,6], without the need of mechanical scanning. Two implementation strategies exists in FD-OCT, i.e., spectral domain OCT (SD-OCT) [5,6] and swept source OCT (SS-OCT) [7,8]. SD-OCT employs a broadband light source and a high speed spectrometer, whereas SS-OCT utilizes a high-speed tunable laser and a photo detector for spectral interferogram detection. Compared to TD-OCT, FD-OCT delivers much faster imaging speed (tens of kilo-Hz vs. several kilo-Hz) [9] due to its improvement in system sensitivity (~20 dB higher) [10,11]. Because of this attribute, the second generation OCT has achieved great success not only in the research arena [12–29], but also in the commercial sectors. Several companies, e.g., Carl Zeiss, Optovue, Heidelberg, Topcon, etc., have marketed different models of the second generation FDOCT systems. All of the current commercial FD-OCT systems can deliver an imaging speed between 27 and 49 kHz, with which it is now possible to provide low definition 3D images of human retina.

Currently, more and more efforts in OCT development have been paid to develop ultrahigh speed FDOCT systems capable of >100 kHz A-line rate, i.e., the third generation OCT. With an imaging speed of >100 kHz, both SS-OCT [30–34] and SD-OCT [35–38] have demonstrated promises for ophthalmic imaging applications. However, compared to SS-OCT, there are several drawbacks in SD-OCT. First of all, most of the ultrahigh speed SD-OCT systems use 850-nm light source, e.g., [35,38]. Though good quality retinal images can be achieved, the 850-nm light is known to have higher tissue scattering property than the light with longer wavelengths. In addition, the system sensitivity is generally lower caused by the shorter exposure time when in ultrahigh speed mode. These attributes make the 850-nm systems difficult to image patients with cataracts and ocular opacities. Furthermore, it is also difficult to image the deep choroidal layers. For the SS-OCT system, 1-µm light source is now typically employed for retinal imaging because it provides deeper penetration than 850-nm light source does due to its lower scattering property in tissue and its low dispersion when propagating through water [39]. Secondly, to realize ultrahigh imaging speed, the SD-OCT systems usually use a linear sensor array with limited number of pixels, resulting in a significantly reduced imaging range (~3.0 mm in air) and rapid sensitivity fall-off (~6 dB/1.5 mm) [35,38]. In contrast, a typical SS-OCT system is capable of offering ~5-mm imaging depth and ~6 dB/3 mm sensitivity fall-off. Further, it is possible for SS-OCT to utilize balanced detection scheme, which gives rise to enhanced system dynamic range. Due to these reasons, most of the efforts in the development of ultrahigh speed FD-OCT now tend to favor the development of the 1-µm SSOCT systems for retinal imaging.

Although the current SS-OCT offers some distinct advantages over the SD-OCT, a number of technical and regulation issues in SS-OCT still remain to be addressed before it can be accepted as the next generation OCT in the marketplace for ophthalmic imaging. First, SS-OCT for clinical use has yet to be approved by the FDA. Since the whole FDA process is time consuming, high risk and expensive, the FDA approval sometimes can be a big barrier for any medical device aiming for clinical applications. Currently, all the FD-OCT systems for clinical ophthalmic use are based on the SD-OCT setup.

Second, for a typical ultrahigh speed SS-OCT system, the captured spectral interferogram is highly non-linear when it is expressed as a function of optical frequency. For example, the fiber-optic Fabry-Perot tunable filter of the FDML laser is driven by a sinusoidal electrical

signal which results in non-linear optical frequency output [33]. To achieve evenly spaced spectral interferograms, usually an auxiliary Mach-Zehnder interferometer (MZI) is required to provide calibration for each individual A-scans [33] due to the dynamic instability of the ultrahigh-speed swept-source system. This requirement would significantly increase the data storage space and demand more data processing power for *in vivo* real-time imaging. Although an optical external trigger generated by the light source may be used to trigger the analog to digital (A/D) acquisition so that the spectral interferogram captured is linear in k space [40], it would significantly decrease the sampling speed of the A/D card (e.g., ~22.5% speed decrease in [30]). This reduction of sampling speed in turn leads to a dramatic reduction of imaging range (from 5 mm to 3.8 mm in [30]). Besides, to the best of our knowledge, there is currently no stable high-speed A/D card [>0.5 Giga sample per second (GSPS)] available that can be triggered using the above method, i.e., the optical trigger. Furthermore, the method in [40] required an A-line interferogram signal (captured in the beginning of the process) as a reference, which is reliable only when the sweep-to-sweep variations are small in slow-speed systems (e.g., 40 kHz in [40]). For an ultrahigh speed SS-OCT, since the sweep-to-sweep spectral interferogram variations are higher, its performance when using the external optical trigger is still questionable [33].

Third, although the SS-OCT systems have the potential to achieve longer imaging range and higher axial resolution simultaneously, it highly depends on the availability of high-speed A/D converter with stable performance (usually multi-channel attribute is also required for the purpose of capturing MZI signal) to capture the spectral interferogram data. For example, in [30], the authors utilized 0.4-GSPS and 1.0-GSPS A/D cards to ensure longer than 5 mm imaging range for the system. In [41], a 2.5-GSPS digital oscilloscope was utilized for data acquisition. All these high-speed data acquisition approaches are very expensive compared to the high-speed Camera Link® interfaces used in the SDOCT systems. Failure to utilize these high-speed A/D acquisitions will result in reduction of either the imaging range or the axial resolution. For example, in [33], a 0.2- GSPS A/D was used for data acquisition, which only provided a 9 μm axial resolution with 2 mm imaging range or a 25 μm axial resolution with 8 mm imaging depth.

Fourth, due to the non-perfect synchronization between the wavelength sweep and data acquisitions, the phase stability of SS-OCT system is relatively poor compared to that of the SD-OCT system, making it difficult to utilize phase-sensitive functional imaging approaches to image blood flows. To stabilize the phases in the SS-OCT systems, additional efforts, in terms of either hardware [42,43] or numerical [44–48] approaches, are required, which would no doubt increase the system complexity and the system computational power.

Finally in terms of clinical translation, the SD-OCT system is more cost effective for current ophthalmic applications. Since all the current commercial ophthalmic FD-OCT systems are based on the SD-OCT setup, the introduction of SS-OCT system will imply a huge investment, e.g., the establishment of a whole new manufacture line. From the above analyses, although SS-OCT is capable of providing promising retinal imaging results, the existing technical and regulatory issues listed above may prevent it from being immediately adopted and developed to become the next generation commercial OCT system in the ophthalmic market. New development of SD-OCT system that is capable of providing comparable system performances to that of a typical SS-OCT system, such as longer imaging range (>5 mm), lower system sensitivity fall-off (~6dB/3mm), deeper penetration depth (using 1 μm wavelength), higher imaging speed (>100kHz A-line rate) and higher axial resolution in air (~10 μm), would be probably more appropriate for the next generation ultrahigh speed OCT systems in ophthalmology.

In this paper, we demonstrate a newly developed ultrahigh speed SD-OCT system that is based on a 1-μm broadband light source and a prototype high speed line scan InGaAs camera capable of 120 kHz line scan rate. The prototype InGaAs camera delivers a 2048 linear sensor array with a pixel size of 10×210 μm^2, making it possible to have comparable imaging

performances to that of a typical SSOCT system. We describe this new SD-OCT system development along with experimental demonstrations of system performances, in terms of the imaging range, the system sensitivity fall-off and its phase stability to image dynamic retinal blood flow. Finally, we show the potential of the SD-OCT system to provide comprehensive assessment of both retina and choroid with a large field of view obtained from healthy volunteers.

2. System configuration

The schematic of the newly developed system is illustrated in Fig. 1, which is similar to that described in [49], except that the system employed a linescan InGaAs camera with 2048 photodiode array that is capable of 120 kHz line-scan rate. Briefly, the system employed a 1050 nm ASE module (Amonics, ALS-1050-20) as the light source, with an output power of ~20 mw. The light module has a 1050 nm central wavelength and 50 nm bandwidth, delivering a measured axial resolution of ~10 μm in air. The output light from the light source was coupled into a 10/90 fiber coupler and split into the reference arm (90%) and the sample arm (10%). In the sample arm, the light was coupled into a custom designed optical probe that contains a collimator, an x-y 2D galvanometer scanning system, an objective lens and an ocular lens. By controlling the galvanometer with different waveforms, the optical probe was able to realize different 2D scans on the posterior part of the human eye. Together with the crystalline lens of human eye, the focus spot of the probe beam at retinal surface was estimated at ~20 μm, which determined the system lateral resolution. Via the 2 × 2 fiber coupler, the spectral interferogram formed between the light backscattered from the human eye and reflected from the reference mirror was recorded by a home-built high-speed spectrometer.
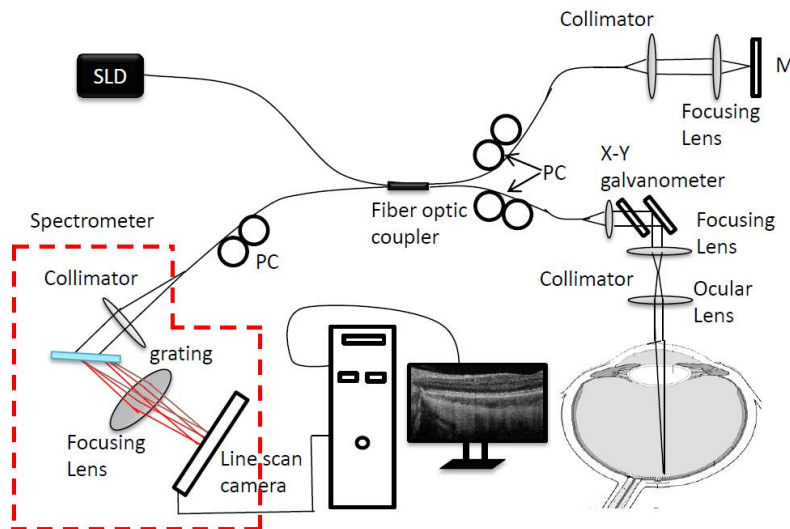

Fig. 1. Schematic of the ultrahigh-speed SDOCT system setup. SLD: 1.0 μm superluminescent diode; PC: polarization controller; M: reference mirror.

The critical improvement of the new system is the implementation of a new prototype high-speed line-scan InGaAs camera (Sensors Unlimited Inc. (SUI), a United Technologies Aerospace Systems company, New Jersey, USA) in the spectrometer. The previously available InGaAs line cameras (model SU1024LDH2) had 1024 pixel array capable of providing the fastest line scan rate of 92 kHz, which has been successfully employed in SD-OCT to image retina, e.g., [49]. However, due to the limited number of the pixel array, the demonstrated SD-OCT system had only ~3.0 mm imaging depth in air and ~6 dB/1.5 mm system sensitivity fall-off [49]. The new SUI prototype camera offers two important improvements: Firstly, the

new camera features an InGaAs photodiode array of 2048 pixels on 10-micron pitch. When it is employed in the spectrometer to cover a light source with 1.05-µm central wavelength and 50-nm bandwidth, the spectral resolution can be significantly higher (~2 times higher) than the previous versions of SD-OCT system, leading to ~6.1-mm extended imaging depth for the prototype system while the system axial resolution is not sacrificed (i.e., maintained at 10 µm in air). Moreover, due to the improvement of the spectral resolution, the spectral bandwidth of the light falling onto one pixel could also be reduced, giving a reduced sensitivity fall off over the imaging depth for the system (see below). Secondly, the new prototype camera, utilizing a Medium Camera Link interface, is capable of much faster linescan rate than the previous SU1024LDH2 cameras (120 kHz vs. 92 kHz), which used a Base CL interface. For in vivo retinal imaging, the imaging speed is an important parameter because the faster imaging speed could minimize the motion artifacts during the *in vivo* experiments. In addition, a shorter examination time is achieved with faster imaging speed, resulting in an improved examination experience for patients.

To evaluate the performance of our newly developed 1-µm ultrahigh speed SDOCT system, a sensitivity experiment was performed. At first, a reflecting mirror was placed in the sample arm to mimic a single layer sample. To reduce the light reflected from the mirror, a 40-dB neutral density filter was installed in the sample arm. Then the reference mirror was moved step by step from 0.1 mm to 6.1 mm (~0.5 mm for each step). At each position, the point spread function was calculated from the recorded interferograms, upon which the sensitivity (signal-to-noise ratio of the peak at each position plus 40 dB) and the axial resolution (full width at half maximum) were evaluated. To compare, a similar experiment was also performed on a SD-OCT system that employed the older InGaAs camera with 92 kHz linescan rate and 1024 pixel array (SU1024LDH2, Goodrich Sensors Unlimited, USA). For the text that follows, we call this previous system as SU1024 system for brevity. The normalized results were demonstrated in Figs. 2(a) and 2(b), respectively. Note that the sensitivity was measured as 100 dB and 99 dB at 0.5 mm position for the new and SU1024 systems, respectively. Figure 2(a) shows the sensitivity fall-off curves obtained from the two systems, where it can be seen that the system fall-off curve for the newly developed system exhibits much slower decay over the imaging depth than the SU1024 system does. The 6 dB fall-off position for the new system is at ~3.0 mm; whereas, the SU1024 system only delivers ~1.5 mm [marked by the black dash lines in Fig. 2(a)]. This improvement is important because it could provide a greater operating flexibility when performing in vivo human eye examinations. With the new system, the system operators would have more freedom to position the micro-structure images in the OCT output plane, thus saving time and minimizing patient discomfort. Figure 2(b) illustrates the measured
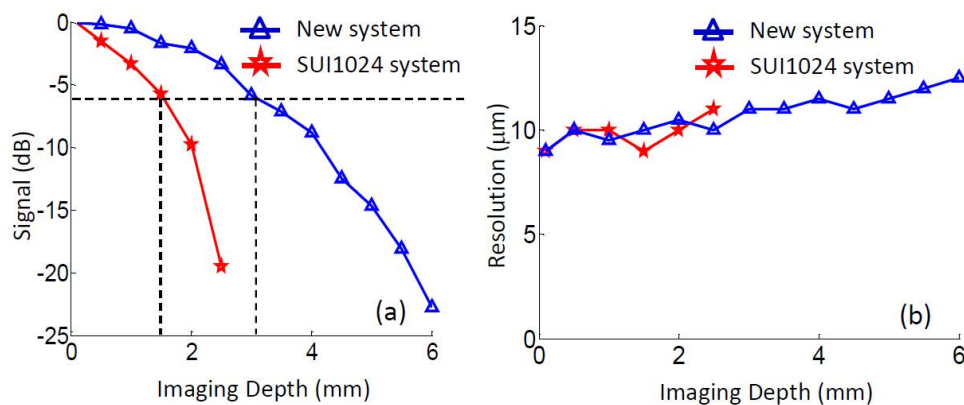

Fig. 2. System performances of the ultrahigh speed SDOCT. (a), system sensitivity fall-off curve of the new system (blue) and the SU1024 system (red). (d) measured system axial resolution at different depth positions for both the systems.

system resolution for the two systems. As seen from Fig. 2(b), the axial resolutions of both systems are almost identical before the 2.5 mm depth, which is about the maximum imaging range of the SU1024 system. After 2.5 mm, the axial resolution of the new system was slightly degraded (from ~10 to 12 μm) due to the achromatic aberration effect of the optic components used in the system setup.

Considering the above, this newly developed SD-OCT system is capable of providing a number of improved system performances while maintaining the axial resolution at ~10 μm in air, which include 6.1 mm extended imaging range, ~6 dB/3 mm system sensitivity fall-off and 120 kHz imaging speed. These system parameters are comparable to a typical SS-OCT system. These attributes together with other advantages (e.g., low cost, easy implementation, and phase stability) may make the SD-OCT system a possibly better alternative for next generation commercial FD-OCT system in marketplace.

3. In vivo eye imaging demonstrations

For better evaluation of the system performance, we performed several *in vivo* imaging experiments using healthy volunteers in our laboratory. In all imaging experiments, the light power used at the eye pupil was ~1.8mW, within the safe ocular exposure limits recommended by the American National Standards Institute (ANSI) [50]. Three experiments were conducted to demonstrate different aspects of the new system. The first experiment was to demonstrate the 6.1 mm extended imaging range and the 6 dB/3 mm sensitivity fall-off of the newly developed system. In this experiment, 1000 A-lines were acquired to form one B-scan, covering ~4 mm on the retina, while the Y-scanner (slow axis) was kept stationary. During the experiment, the reference mirror was carefully adjusted so that the retinal microstructure image formed by the system was positioned at ~1.0, 2.5, 4.0 and 5.0 mm depth locations of the system, respectively. For comparison, we also performed a similar experiment using the SU1024 system. Due to the limitation of the imaging range of this system, we only acquired the retinal microstructural images at two depth locations (1 mm and 2 mm, respectively).

The second experiment was used to demonstrate the phase stability achieved by the new SD-OCT system. A high density A-scan protocol was designed to extract the phase information due to the blood flow within human retina. For this, we captured 2500 A-lines within one B-scan, covering 3 mm length on the retina. Considering the lateral resolution of our system (~20 μm), this configuration provided >90% overlap between adjacent A-lines, which meets the requirement for phase-resolved optical Doppler tomography (PR-ODT) evaluation of blood flow. When using an 80% duty cycle to drive the X-scanner, the system was run at 38 frames per second. 200 repeated B-scans (i.e., time-lapse B-scans) were captured from one fixed position during the experiment.

The third experiment was designed to achieve a 3D visualization of human retina in a large field of view. For this experiment, X-Y scanner was enabled to acquire 3D data set from the retina. In the fast scan direction, 720 A-lines were captured to form one B-scan, which covered ~10 mm length on the retina. In the slow-scan direction, 720 B-frames were also captured, covering ~9 mm length on the retina. When the X-scanner was driven by an 80% duty cycle saw tooth waveform, the system imaging speed was 130 frames per second. With this speed, it required ~5.5 seconds to complete one 3D scan of 10x9 mm^2.

For all the experiments reported here, the head of the volunteer was placed on a customized examination stage for stabilization. During the experiment, the volunteer was asked to stare at an aiming target in order to minimize the eye movements. All the experiments were performed in a dark room to help enlarge the pupil size.

3.1. In vivo B-scan microstructural images at different depth locations

Since the imaging sensitivity is gradually decreased when the sample moves away from zero-delay line [Fig. 2(a)], the best imaging range for a typical SD-OCT system is usually at the region where the system sensitivity fall-off is less than 6 dB. The longer imaging range and the
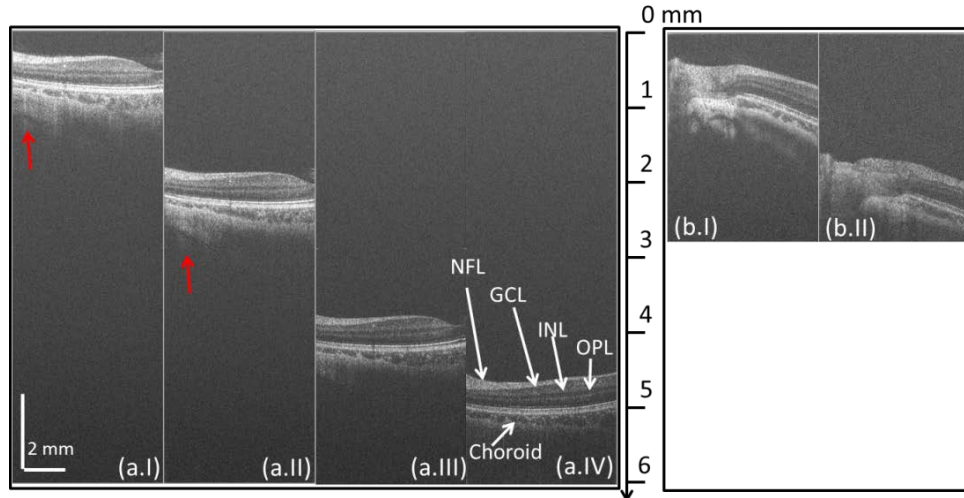
Fig. 3. In vivo B-scan retinal images at different depth locations captured by (a) the new system and (b) the SU1024 system. (a.I)–(a.IV) are the B-scan images captured at the positions of 1 mm, 2.5 mm, 4 mm and 5 mm, respectively. (b.I) and (b.II) are the B-scan images captured at the positions of 1mm and 2 mm, respectively. NFL: nerve fiber layer; GCL: gaglion cell layer; INL: inner nuclear layer; OPL: outer plexiform layer.

lower system sensitivity fall-off that a FDOCT system possesses, the more flexible is for in vivo human eye imaging. This is because the operator would have better chance to operate the system that can generate good quality images, even when the target moves (in a small amount) during the experiments. The advantage of the new system over the SU1024 system is clearly demonstrated in Fig. 3.Figure 3(a) demonstrates four images, (a.I), (a.II), (a.III), and (a.IV), which were acquired when the human retina was located at the depth positions of approximately 1 mm, 2.5 mm, 4 mm, and 5 mm away from the zero-delay line, respectively. As we can see, even at 5 mm depth position (almost at the end of the imaging range, Fig. 3 (a.IV)), the new system still produced high contrast retinal image, in which all the important retinal layers, such as nerve fiber layer (NFL), outer plexiform layer (OPL) and choroid, were visualized (labeled in Fig. 3 (a.IV)). However, due to the sensitivity fall-off of the system, Fig. 3 (a.IV) shows much lower image quality and contrast compared to Fig. 3 (a.I) and (a.II) (close to the zero delay line). The signal coming back from deep sclera layer (pointed by the red arrows) are also strong in Fig. 3 (a.I) and (a.II) with excellent contrast, whereas for Fig. 3 (a.III) and (a.IV), the sclera layer demonstrates lower contrast due to the lower system sensitivity at deeper depth positions. The four images in Fig. 3(a) illustrate that the best imaging region of our new camera system is from zero delay line to 3 mm depth position, where the sensitivity fall-off is less than ~6 dB. For comparison, the imaging results obtained from the SU1024 system were given in Fig. 3(b). Compared to Fig. 3(a), there are two major drawbacks of the SU1024 system. At first, the imaging range of the SU1024 system is only ~3 mm. If the sample is positioned beyond this range, the system would fail to see the sample. However, for the new system, the imaging range is extended to 6.1 mm. Even at the position of 5 mm (Fig. 3 (a.IV)), the sample can still be visualized. Second, the sensitivity fall-off of the new system is much slower than the SU1024 system. For the SU1024 system, only when the sample is located at around 1 mm region, a good quality image is observed (e.g., Figure 3 (b.I)), which makes it harder to operate the SD-OCT system to obtain satisfactory retinal images, particularly when the subject is in constant movement, which is inevitable for in vivo imaging. For the new system, good quality images can still be obtained when the sample is located at ~3.0 mm (Fig. 3 (a.II)), giving the operator more flexibility to operate the system.

3.2. In vivo phase resolved Doppler imaging of blood flow within human retina

The capability to resolve phases is very important for the OCT system because it extends the function of OCT to image the blood flows and the tissue motion within living tissue [51]. Briefly speaking, the principle of phase-resolved technology is based on the well-known Doppler effect. When the light backscattered from a moving particle, it will carry a Doppler beating frequency. If the movement of the particle is small (< one half of the wavelength in one direction), then the beating frequency can be estimated by calculating the phase difference between adjacent A-lines. Since it was proposed in [51], this phase-resolved technology has been successfully applied for blood-flow imaging [51,52], tissue Doppler imaging [53], photo-thermal imaging [54,55], and so on. Especially, if the movement of the particle is periodic, these techniques have been demonstrated to have sub-nanometer scale sensitivity when combined with frequency analyses [54–56]. To perform phase Doppler evaluation, the utmost requirement is the phase stability of the system. Low system phase stability would certainly deteriorate the imaging sensitivity to the movement. Currently, the SD-OCT system delivers better performance on the phase stability than the SS-OCT system does, which makes SD-OCT better suited for functional phase sensitive applications. Though SS-OCT has been demonstrated to have phase-resolved capability [42–48], it needs additional investments either in hardware or in software, which will no doubt increase the system complexity and cost. In this section, the results obtained from the second experiment were used to demonstrate phase stability of the system and its ability to evaluate dynamic retinal blood flow.

Figure 4(a) presents a typical cross sectional image captured across human optic nerve head using the new ultrahigh speed SD-OCT system. Figure 4(b) is the corresponding bi-directional Doppler flow map, obtained by calculating the phase differences between adjacent A-lines. From Fig. 4(b), several blood vessels can be clearly identified (e.g., vessel numbered as 1 and 2 pointed by the white arrows in Fig. 4(b)). In Fig. 4(b), the black color means the flow direction is towards the probe beam while the white color is away the probe beam. As suggested by previous studies [57–59], the hemodynamics of retinal blood flow plays an important role in a number of eye diseases, such as glaucoma, diabetic retinopathy and age-related macular degeneration. Although some parameters such as flow volume are difficult to obtain directly through a simple M-mode scan due to the limitation of Doppler angle dependence, the quantification of pulsatile flow pattern is a valuable alternative for the analysis of flow dynamics, from which several parameters (e.g., pulsatility index, resistance index and so on) may be estimated [60]. To evaluate the pulsatile flow, the phase difference value was integrated within the blood vessels numbered 1 and 2 in Fig. 4(b), respectively. The result is demonstrated in Fig. 4(c), where the red and blue curves indicate the integrated phase difference values of vessels 1 and 2, respectively. For comparison, the values plotted are the absolute values. From Fig. 4(c), the cycles of the heart beat can be clearly visualized. More than three cycles were demonstrated in this figure. The blood flow pattern of the number 1 vessel is oscillatory with much higher and sharper peak than that of the number 2 vessel, the behavior of which is an expected pulsatile pattern from an artery. On the other hand, over a period of time investigated, the pulsatile flow pattern in the other vessel (vessel number 2) is obviously lower and has a phase lag with respect to the arterial flow of the vessel number 1, which is a representation of a venous flow.
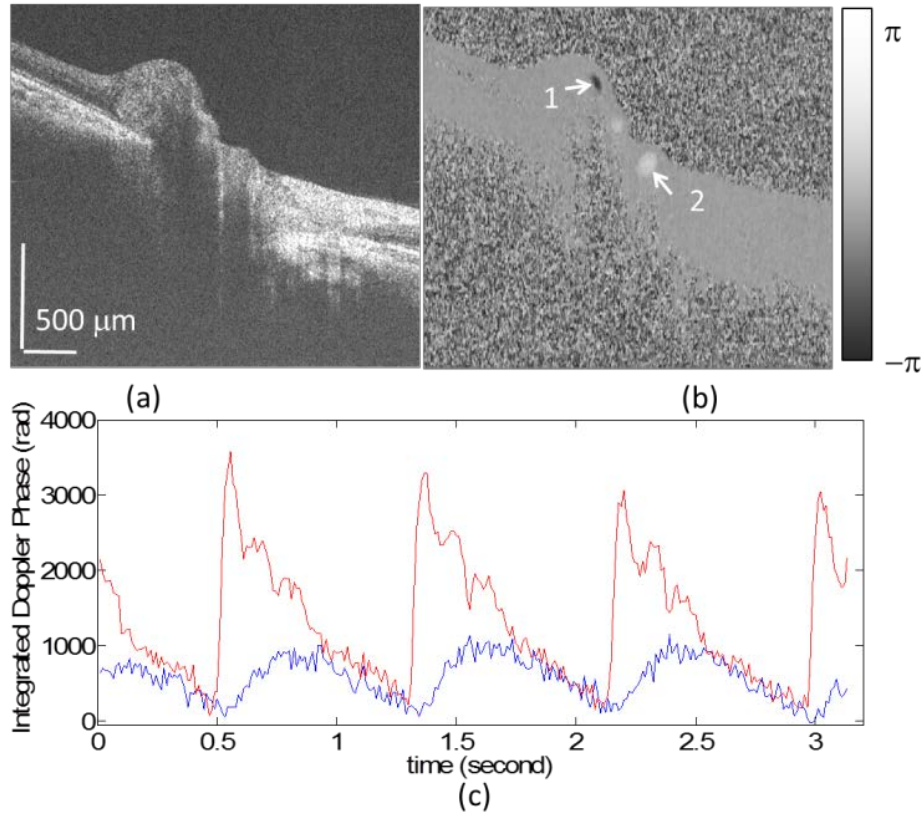
Fig. 4. In vivo evaluation of the dynamic retinal blood flow. (a) a typical B-scan image across optic disc. (b) the corresponding phase difference map calculated through the phase resolved technology. (c) retinal blood flow dynamic curve. The red curve corresponds to vessel 1 (artery) and blue one to vessel 2 (vein).

3.3. In vivo large-field-of-view imaging of posterior segment of human eye

A capability of scanning a large field of view is very important for an ophthalmic OCT system, because it could offer comprehensive assessment of the scanned tissue status quickly, as well as much flexible analysis and quantification of the interested features within the scanned region. Though the second generation system has already demonstrated 3D imaging capability, the sampling density has to be sacrificed due to the limitation of scanning time (usually couple of seconds) caused by the limited imaging speed [12–29]. The less sampling density would certainly increase the possibility of missing small abnormal features when performing the eye examination. With the proposed ultrahigh speed SD-OCT system, it is able to obtain high definition 3D imaging from a large field of view. To demonstrate, a 3D scanning protocol previously mentioned was used to capture a 3D data representing an area of 10×9 mm^2 on the retinal surface.

Figure 5(a) is the OCT fundus image, obtained by integrating the captured A-lines along the z-direction. With the large field of view, it is possible to survey the overall status of the retina. Several big blood vessels can be visualized. Figure 5(b) is 3D volumetric rendering image of the captured data, which is supposed to provide more depth related information about the retina and choroid of human eye. However, due to the inevitable subject movement during imaging as well as the obvious retinal curvature, the image quality is severely deteriorated. For better visualization (e.g., depth resolved en-face view), a compensation approach can be used to eliminate the motion artifact.
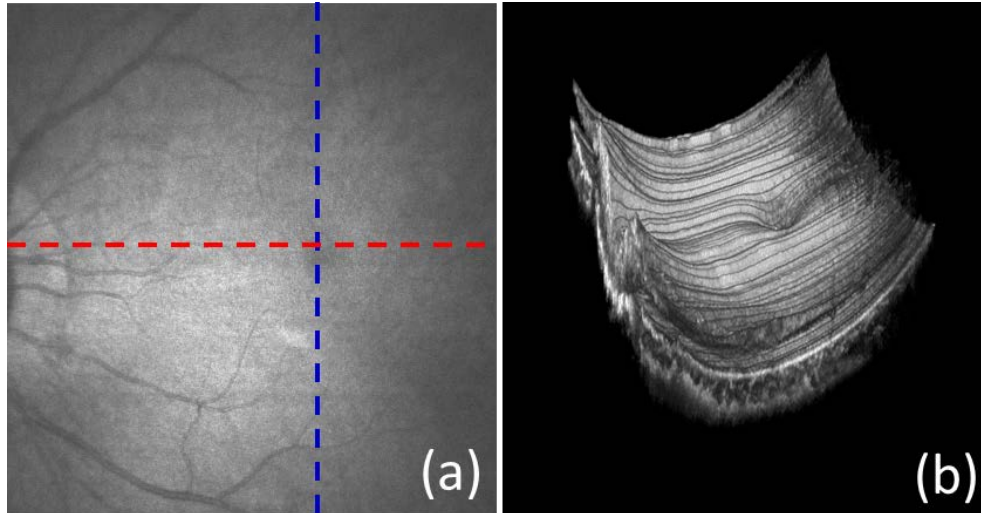
Fig. 5. In vivo large field of view retinal and choroid imaging with a scanned area of 10×9 mm^2.
(a) OCT fundus image; (b) 3D rendering volumetric image.

Figure 6(a) is a typical cross sectional image along Y-direction (slow axis), which was extracted from the 3D data set. The position for Fig. 6(a) is marked by a blue dash line in Fig. 5(a). Due to the movements of the subject (the fluctuation pattern), it is difficult to directly extract the valuable information from Fig. 6(a). Figure 6(b) is a typical cross section image along X-direction, i.e., the fast axis (marked by a red dash line in Fig. 5(a)) where curvature pattern (marked by a red curve) is obvious although the motion artifact is minimal. To compensate these two effects, two strategies were performed. At first, a cross correlation method was used to calculate the displacement between adjacent B-frames. In order to increase the calculation speed, a small window was first created (e.g., the white square in Fig. 6(b)). Since the position of the retina was changed due to the subject movement, a special attention was paid to the selection of the small window, which should cover some microstructure features within all frames of a 3D data set. The image covered by the small window (presented as Fig. 6(c)) was used to calculate the cross correlation with the first B-frame within the 3D data set. The peak position of the cross correlation map (marked by the white arrow on Fig. 6(e)) indicates the movement amount, upon which the displacement between the selected frame and the first frame is calculated and consequently compensated. Because the captured data covered a large field of view, when the selected frame is far away from the first frame, it will be difficult to obtain an accurate correlation peak position due to different microstructural appearance along with the slow axis. To solve this problem, the data set captured by our system was evenly separated into 20 sub-data sets along the slow axis. The displacements within the sub-data sets were first compensated using the cross correlation method. Then, the displacements between adjacent sub-data sets were compensated by calculating the cross correlation between the first frames in the each sub-data sets. After the above process, the movements were successfully compensated. Figure 6(d) demonstrates a typical cross sectional image along the slow axis after the motion correction. As we can see, the fluctuation pattern was successfully eliminated, giving a similar image quality to that of B-frames along the fast axis (e.g., Fig. 6(b)).
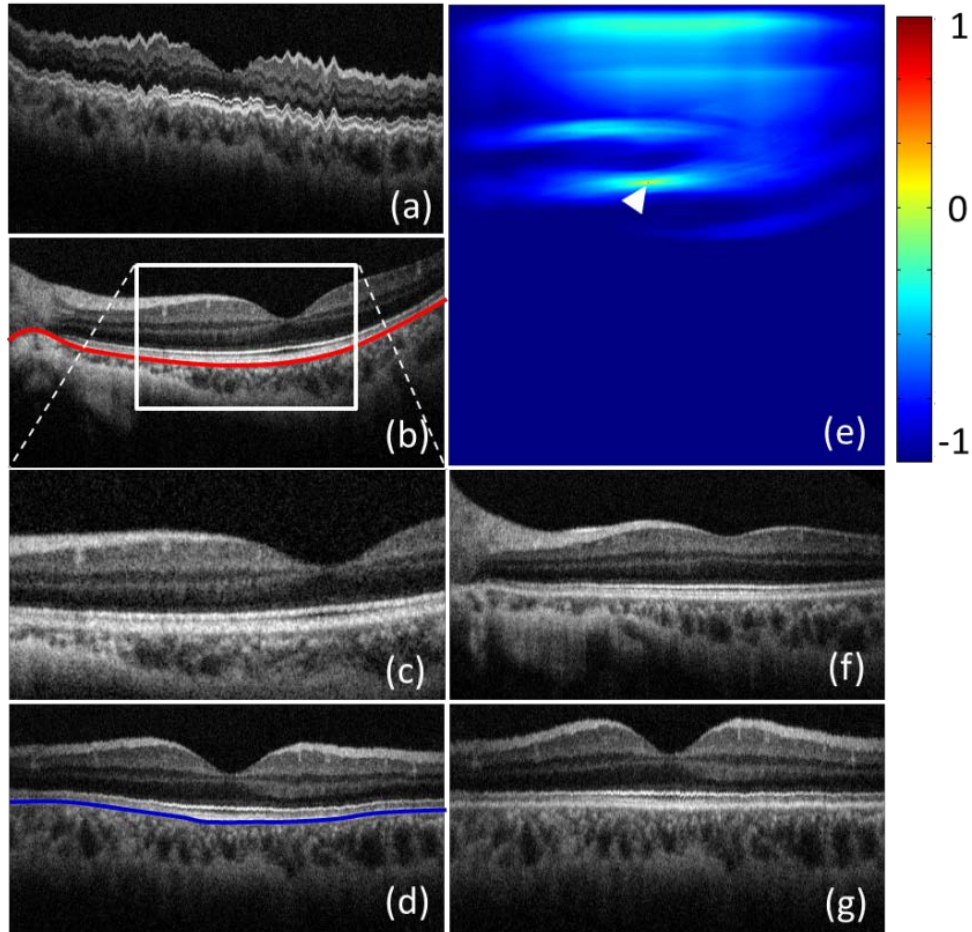
Fig. 6. Motion and curvature compensation for 3D image data set. (a) Typical cross sectional image along the slow scan axis; (b) typical cross sectional image along the fast scan axis; (c) zoomed cross sectional image covered by a selected window for motion compensation; (d) typical cross sectional image after motion compensation along the slow scan axis; (e) typical cross correlation map between two B-scan images; (f) typical cross sectional image after compensating the retina curvature along fast axis; (g) typical cross sectional image after compensating the retina curvature along the slow axis

After motion compensation, the second step is to apply a flattening operation to eliminate the curvature appearance of the frames. In doing so, the retinal pigment epithelium (RPE) layer in each B-frame along the fast axis (e.g., the red curve in Fig. 6(b)) was first extracted and used as the reference to flatten the B-frame images (e.g., Fig. 6(f)). Then, a similar process was repeated along the slow axis to compensate the Y-direction retinal curvature (e.g., the blue curve in Fig. 6(d)). Figure 6(g) shows a typical cross sectional image along the slow axis after retinal curvature correction. As evident from Figs. 6(f) and 6(g), the 3D data set is now flattened along both the directions and is ready to be analyzed further.

Figure 7(a) demonstrates the 3D volumetric rendering of the data set after flattening process along both fast and slow axes according to the RPE layer. Compared to Fig. 6(b), several important microstructural patterns within the posterior segment can now be appreciated, such as fovea (FV), parafovea (paraFV), perifovea (periFV), optic nerve head (ONH), choroid layer and so on. In addition, due to the depth-resolved nature and high resolution characteristics, these morphological features may be qualitatively or even quantitatively evaluated. For example, the choroidal thickness near the fovea region is thicker than that near the ONH
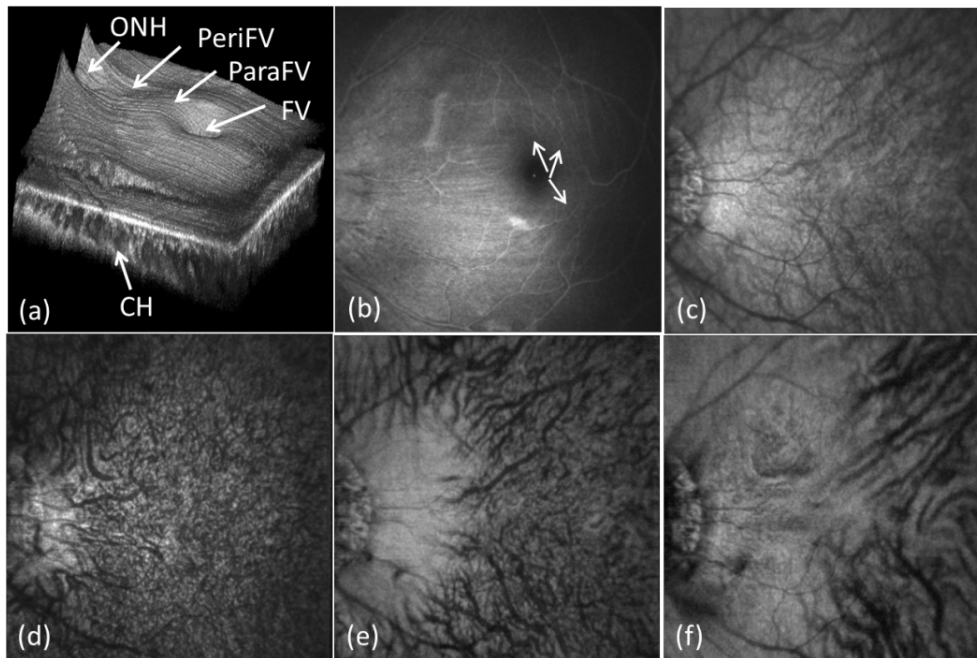
Fig. 7. In vivo large field of view retina and choroid imaging results after compensation. (a) 3D volumetric image; (b) retinal fundus image obtained though integrating between 20 and 250 mm above the RPE layer; (c) choroidal fundus image obtained through integrating between 10 and 250 mm below the RPE layer; (d-f) depth resolved choroid fundus image obtained through integrating from 5 to 30 μm, 30 to 100 μm and 100 to 250 μm below the RPE layer, respectively. See also Media 1.

region. For further analysis, some images were created through integrating the microstructural signals at different depth locations along Z-direction. The results are presented in Figs. 7(b)–(7f). Figure 7(b) is the retina projection image obtained through integrating the microstructural signals from 250 μm to 20 μm above the RPE layer. Compared to Fig. 5(a), the retina blood vessels (not only the bigger vessels, but also some smaller vessels) can now be visualized (pointed by the white arrows in Fig. 7(b)). Figure 7(c) is the projection image of the choroidal layer corresponding to the position from 5 μm to 300 μm below the RPE layer, where the abundant choroidal blood vessels are seen. For better visualization, the choroid layer was further divided into three layers according to their depth locations. For each layer, a projection image was produced through integrating the microstructural signals along the Z-direction within that layer. The results are demonstrated in Figs. 7(d)–(7f), corresponding to the depth position from 5 to 30 μm, 30 to 100 μm and 100 to 250 μm below the RPE layer, respectively. From these images, the different sizes of blood vessels within three typical choroidal layers (chorocapillaris layer, Sattler's layer and Haller's layer) can be appreciated. For example, the chorocapillaris layer is filled with the smallest micro-capillaries while the Haller's layer contains bigger vessels. The associated movie (Media 1), which gives flying en-face views from the anterior retina to the posterior choroid, provides detailed visualization of the microstructures at different depths. The performance demonstrated by the proposed system suggests that it may serve a potential diagnostic tool for future clinical applications.

4. Conclusion

We have demonstrated a newly developed high-speed 1050 nm SD-OCT system based on a new prototype high speed line-scan InGaAs camera. We have experimentally shown that this new system is capable of an axial resolution of 10 μm in air, an imaging range of 6.1 mm in air, a system sensitivity fall-off at 6 dB/3 mm, and an imaging speed of 120,000 A-lines per second,

which system performance parameters are comparable to that of a typical 1μm SS-OCT used for imaging the posterior segment. We have also shown that the proposed system has enough phase stability to perform imaging of dynamic blood flow within retina. The phase stability of the system is an important parameter for any OCT system because it extends the conventional OCT system into functional imaging of blood flow dynamics as well as the tissue movement. With an imaging speed of 120 kHz, we demonstrated the proposed system is capable of providing a large field of the posterior segment of the human eye, an important attribute for retinal imaging because a large of field of view provides an opportunity to quickly survey the retinal status during the eye examination.

Acknowledgments